Journal of Sea Research 74 (2012) 26–34

Contents lists available at SciVerse ScienceDirect

Journal of Sea Research

journal homepage: www.elsevier.com/locate/seares

Ship-borne contour integration for flux determination

Sjoerd Groeskamp, Leo R.M. Maas *

NIOZ Royal Netherlands Institute for Sea Research, P.O. Box 59, 1790 AB Den Burg, The Netherlands

ARTICLE INFO

Article history:
Received 13 September 2011
Received in revised form 27 April 2012
Accepted 7 May 2012
Available online 6 June 2012

Keywords:
Tidal dynamics
Estuary
ADCP
Mussels
ADCP
Contour integration

ABSTRACT

The consumption of nutrients by mussel beds can be monitored by measuring the net nutrient flux across a circumscribing vertical surface. Measuring this nutrient flux not only requires resolving the spatial (and temporal) distribution of nutrients at the bounding contour, but also an ability to unambiguously measure net water motion across it. As a prerequisite for future application to nutrient flux determination, we here describe results of a field campaign in the inland Wadden Sea in which we aim to measure just the latter water balance. This is done by comparing the water transport across a vertical surface, spanned by the closed contour and the bottom, to the net tidal displacement of the free surface enclosed by this contour. The former is obtained by measuring currents while traversing the contour repeatedly within one tidal cycle. The latter is estimated using sea-level observations at nearby tidal stations as well as by means of direct sea-level observations at the location of measurements. The current measurements are used to reveal the spatial structure of the tidal and tidally rectified fields, which are divided into cross and along contour currents. These measurements show how the presence of a steep slope in the bathymetry has an impact on the presence of circulation cells that are relevant for the mixing and flushing of water. A neat closure of the water budget is obstructed since it is dominated by the difference between a strong inflow and a concurrent, nearly equally strong outflow. For future application we recommend using observed tidal elevations within the closed contour as a constraint in determining the best estimates for cross-contour water fluxes, thus opening the route to genuine nutrient flux measurements by 'contour integration'.

1. Introduction

Mussel beds, intended for mariculture, occupy large areas of the bottom of inland seas. Catchment of mussel seed from such beds leads to the inadvertent destruction of other marine life. An alternative, less destructive and perhaps also more fruitful method to grow mussel seeds, is presently tested in the Dutch part of the Wadden Sea. This is done by growing them on hanging long-lines. The 300 m long nets have a 4 cm maze and are suspended vertically over a 3 m range from surface floats. The floats are attached to poles that are anchored to the bottom. In this way, the seeds of bivalve suspension feeders (*Mytilus edulis*) are grown. These seeds are harvested once they are about 5 mm in size and are then moved for further nurturing to intensive mussel farms, where they are raised to adult size. In the Western Wadden Sea, five sets, of 4 to 6 such long-lines each, are suspended. The individual long-lines are aligned in sets that are oriented in the dominant current direction, as shown inside the ellipse in Fig. 1. Together these comprise a 'mussel seed installation' (MSI). The MSI under consideration in this study is located at the side of Malzwin channel, a 12 m deep tidal channel oriented in a direction 55°T (True North), roughly from SW to NE (see Fig. 1). The channel is located beside a shallow shelf of about 5 m depth, lying to the South East. A recent discussion of the hydrodynamics of the Western part of the Dutch Wadden Sea, a tidal estuary separated from the North sea by a chain of barrier islands, is given e.g. in (Groeskamp et al., 2011).

One of the concerns regarding this new mussel breeding technique is local overconsumption of nutrients, producing 'aqua deserts' in the immediate vicinity of the installations. In order to quantify the amount of nutrients fixated over a certain period of time, and to see to what extent this affects the surroundings, an effective monitoring strategy is looked for.

The applied monitoring strategy consists in measuring hydrodynamic and environmental parameters over one tidal cycle using a vessel that moves repeatedly along a fixed track that circumscribes the MSI, each single track taking less than 30 min (see Fig. 2). Employing Gauss' divergence theorem, and treating each circuit as instantaneously covered, one can infer the transport through the vertical surface bounded by the traversed contour at the surface and the bottom. Dividing this transport by the area of this vertical surface we obtain the flux into or out of the enclosed volume. Because the transport is measured repeatedly from one circuit to the next, one can follow its changes over a tidal period.

Employing Green's theorem to the along-contour depth-averaged velocity allows determination of the average vorticity, where averaging is over the area enclosed by the circuit. This quantity contains information on the tidal and tidally-averaged shear, both of relevance to the mixing.

* Corresponding author.
E-mail address: maas@nioz.nl (L.R.M. Maas).

1385-1101/$ – see front matter © 2012 Elsevier B.V. All rights reserved.
doi:10.1016/j.seares.2012.05.007

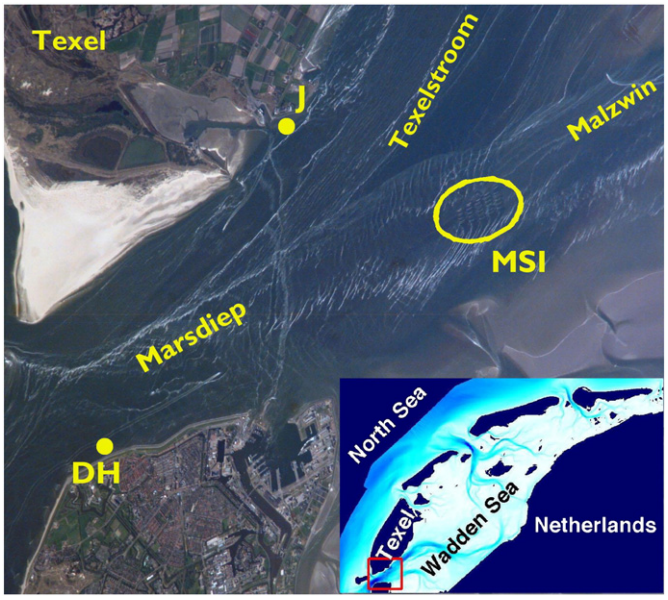

Fig. 1. Astronaut photograph on board the International Space Station of the Western Dutch Wadden Sea, 1st of May 2007. The yellow ellipse gives RV Stern's trajectory of 26 subsequent circuits within one tidal period around mussel seed installation (MSI). Within the ellipse, five North–south oriented sets of long-lines can be observed, on which mussel seed is growing. Sea surface height is measured at Den Helder (DH) and at the jetty (J) at Texel Island, the Netherlands.

Our strategy for finding nutrient fluxes by rapidly moving around an MSI while measuring pertinent quantities was here first tested without any living mussel seed in place. Our ability to estimate net exchanges over the curve sailed during one circuit was therefore tested on a physical (hydrodynamic) property, i.e., the net water transport. Over the duration of a tidal period, 26 cycles were completed during which the velocity field was measured continuously over the full depth. Over each single loop the net mass transport into the loop was obtained by integrating over the closed contour, i.e., by adding the mass transport across the 32 compartments constituting the closed contour. This transport determines the actual sea level change taking place inside the contour provided that over the course of one circuit no significant rain, evaporation or seepage through the bottom has taken place. We will compare this net transport to the net change in sea surface height over the duration of each single loop, obtained by other means.

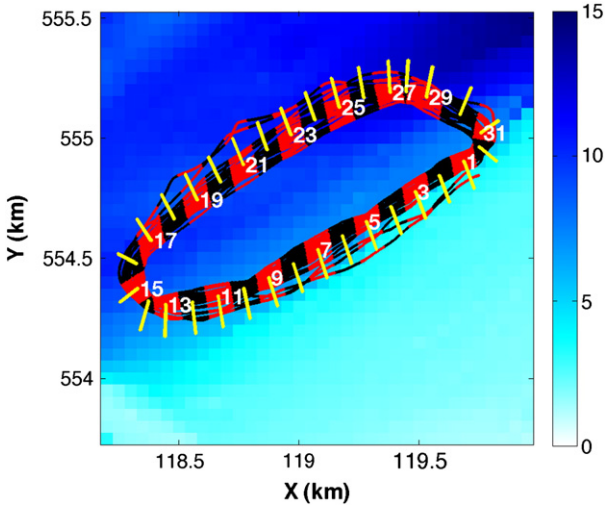

Fig. 2. Zoom of RV Stern's circuits in an East-North oriented *x,y* frame expressed in Parisian coordinates (see text). Data collected within 32 compartments (white numbers), colored alternatingly black and red, are combined. Observations in these compartments are attributed to the central grid points; sticks indicate normal direction to the average contour. Background color represents water depth in m (see color table).

Thus we arrive at the following goals: our first aim is to describe and discuss the application of our monitoring strategy, with the purpose of estimating fluxes through and circulation around the contour sailed by a vessel. Our second aim is to apply this strategy to the measured velocity field and to infer properties of the tidal and tidally-averaged fields, relevant to the mixing near the MSI.

In Section 2 of this paper we will briefly discuss the collected data set. Section 3 discusses how contour integration methods can be used on data coming from our applied monitoring strategy. In Section 4 we discuss tidal dynamics extracted from our data set and explain what inferences can be drawn in applying 'contour integration'. Finally, Section 5 provides a discussion on applying the contour integration method in case a nutrient source or sink is present within the enclosed volume, and we give recommendations for future studies. We end Section 5 with some conclusions.

2. Data collection

Measurements of position, water depth, currents and fluorescence were performed continuously during one tidal cycle, both on 6 and 9 October 2009, respectively. In this paper we will discuss only current measurements starting at 04:37 GMT of 6 October (day 279), finding those of the second cruise to be similar.

Continuous onboard measurements are obtained either near the surface, such as of nutrients, or over the full water depth, as in the case of velocity measurements, using an Acoustic Doppler Current Profiler (ADCP). This provides 3D velocities along the vertical surface spanned by the closed contour that the ship traverses and the bottom. Combining these along-contour data allows the determination of net transport across the circumscribing surface over the duration of subsequent circuits. Upon division by the vertical surface area this yields the net flux. To measure position and water depth, we use an onboard global positioning system (GPS) and echo sounder. The other parameters are obtained by sensors attached to a pole that is stuck in the water from the side of RV Stern. The pole is equipped with a 1200 KHz Workhorse Rio Grande ADCP and a Sea-Bird Electronics CTD.

The ADCP operates at 1 Hz. The experimental setup made it impossible to accurately determine the heading misalignment (α) between ADCP and Ship coordinates beforehand. Joyce (1989) provides a method to correct for both α and the beam orientation (β). The method assumes a constant velocity in time, while crossing a particular place multiple times, and it does not take into account the effects of trajectory curvature. These conditions do not apply for the current study, so that we have used the difference between the direction given by the GPS and the bottom tracking to obtain $\alpha = 41.56° \pm 1.07°$. Following (Joyce, 1989), beam correction factor β is calculated using $1+\beta = 1-\Delta\phi \cot\phi = 0.956$, where $\phi = -70°$ is the beam angle with the horizontal and $\Delta\phi = -0.12°$ is the deviation of a beam pair from this angle. The data is corrected using

$$u = (1+\beta)\left[u' \cos\alpha - v' \sin\alpha\right]$$
$$v = (1+\beta)\left[u' \sin\alpha + v' \cos\alpha\right]$$

where u' and v' are the water velocities in east and north ADCP coordinates, corrected for the ship velocity. These data are subsequently averaged in a manner described next.

2.1. Averaging

We take the average position of the $J = 26$ loops that are traversed as reference. To do so, we define $I = 32$ compartments (red and black areas in Fig. 2) and attribute any observation in each of these compartments to their centers. These are situated at 'Parisian positions'

$\mathbf{X}_i = (X_i, Y_i)$, $i \in \{1, I\}$, a Cartesian location that takes Paris as geographical reference. Then we define the average Parisian position of the whole reference loop: $\mathbf{X} = I^{-1}\sum_{i=1}^{I} \mathbf{X}_i$. This leads to local centered coordinates of the grid-points $\mathbf{x}_i = \mathbf{X}_i - \mathbf{X}$. By definition, their average position is zero and the coordinates range up to 1500 m. Because of the J loops, the observations in the grid boxes provide time series of depths H_{ij}, $j \in \{1,J\}$, Optical Back Scatter, and surface measurements of temperature T_{ij}, salinity and other scalars, such as nutrient concentration. These are given at times t_{ij} at which these fields are sampled in grid-point i during the j-th cycle. We choose an origin of time, $t = 0$, that starts at the moment that the first average in the first grid point ($i = 1$) is determined, a little later than the actual first measurement. Thus, $t = 0$ corresponds to 6 October 2009, 04:45 GMT. We also have observations of the velocity *vector* field $\mathbf{u} = (u, v, w) = \mathbf{u}_{ijk}$ in depth bin k. During the j-th loop, this is measured at position $\mathbf{x}_i$ from surface-bin, $k = 1$, down to the maximum bin, $k = K_{ij}$, determined by water depth H_{ij}. The output depends of course on tidal phase.

In subsequent analysis we determine directional vectors along the loop, $\mathbf{ds}_i = (\mathbf{x}_{i+1} - \mathbf{x}_{i-1}) = (dx_i, dy_i)$, and normal to the loop, $\mathbf{dn}_i = (-dy_i, dx_i)$ (see Fig. 2) and the unit normal vector $\mathbf{n}_i = \mathbf{dn_i}/|\mathbf{dn_i}|$. Here dx_i and dy_i denote displacements in the East and North directions in grid point i, respectively.

The time-averaged depth in each center-point, denoted by a tilde, is found by averaging over the 26 cycles: $\tilde{H}_i = J^{-1}\sum_{j=1}^{J} H_{ij}$ (see Fig. 3a, to be read in conjunction with Fig. 2). The average depth shows that grid points 1–13, and 31–32 are located over shallow (5–6 m deep) water, while grid points 17–29 are over deep water (10–12 m). The remaining grid points are over the connecting slope. The temporal variation of the spatially-averaged depth, relative to the spatially and time-averaged depths, $\zeta_j = I^{-1}\sum_{i=1}^{I} \left(H_{ij} - \tilde{H}_i\right)$, represents the sea surface elevation at the MSI (see Fig. 3b). In this figure they are shown together with sea surface elevations observed on the neighboring shores (see Fig. 1). Compared to sea surface elevation measurements at the MSI, those onshore have slightly smaller tidal amplitudes and reach tidal maxima a bit earlier. Both effects are due to side wall friction. The sea level elevation observed at the average MSI position may further on serve as a reference against which we can test our ability to close a water balance using measured water transport across the bounding contour.

3. Contour integration methods

We will be applying two well known methods to access fluxes in the field by employing our observations of the velocity field along the closed contour traversed by the ship. Because this leads to integrals along a closed path, in mathematics referred to as a line or contour integral, we will here call these 'contour integration methods' as well.

The first method employs Gauss' divergence theorem. This theorem says that the integral of the divergence of a vector field $\mathbf{u}$ over a fixed volume V equals the integral of the normal component of that field through its bounding surface ∂V:

$$\int_V \nabla\cdot\mathbf{u}\ dV = \int_{\partial V} \mathbf{u}\cdot\mathbf{n}\ dA.$$

Here $\mathbf{n}$ denotes an outward directed unit vector normal to surface ∂V. We can apply this principle to a volume V that is bounded by a surface ∂V composed of ∂V_1, the vertical surface whose intersection with the free surface is the closed contour traversed by the ship (on which surface the velocity field is measured), ∂V_2, the enclosed bottom (whose impermeability implies there is no flow through the bottom), and ∂V_3, the enclosed, temporally and spatially-averaged sea level. Since water is (nearly) incompressible and the velocity field $\mathbf{u}$ thus nondivergent, the left hand side of this equation vanishes. Thus we are left with:

$$\int_{\partial V_3} \mathbf{u}\cdot\mathbf{n}\ dA_3 \approx \frac{\partial \zeta}{\partial t} A_3 = -\int_{\partial V_1} \mathbf{u}\cdot\mathbf{n}\ dA_1,$$

where ζ is the sea surface elevation with respect to the temporally and spatially averaged sea level, that is assumed uniform over the enclosed surface area $A_3 \equiv \partial V_3$. The 'contour integral' on the right hand side thus tells us that a net inflow through vertical bounding contour ∂V_1 should be compensated by an equal outflow through mean horizontal surface, ∂V_3, or vice versa. The latter outflow manifests itself as the local time rate of change of the average sea surface elevation within the enclosed contour. Since this surface elevation can also be obtained from external sources, such as from tide gauges in the proximity of the contoured area, this provides us with a test of the accuracy with which the net volume transport through ∂V_1 can be measured using our ship-borne contour integration method.

The second method employs Green's theorem. This says that the strength of a vortex tube, the integral of the normal component of the vorticity field $\boldsymbol{\omega} = \nabla \times \mathbf{u}$ over surface A, bounded by contour ∂A, equals the circulation around this contour:

$$\int_A \boldsymbol{\omega}\cdot\mathbf{n}\ dA = \oint_{\partial A} \mathbf{u}\cdot\mathbf{ds}.$$

Here $\mathbf{ds}$ is an incremental element along curve ∂A. Thus, by measuring the circulation around the contour, represented by the contour integral, we can infer the average vorticity of the area enclosed by it. In the next section we apply the two theorems on our data set – we

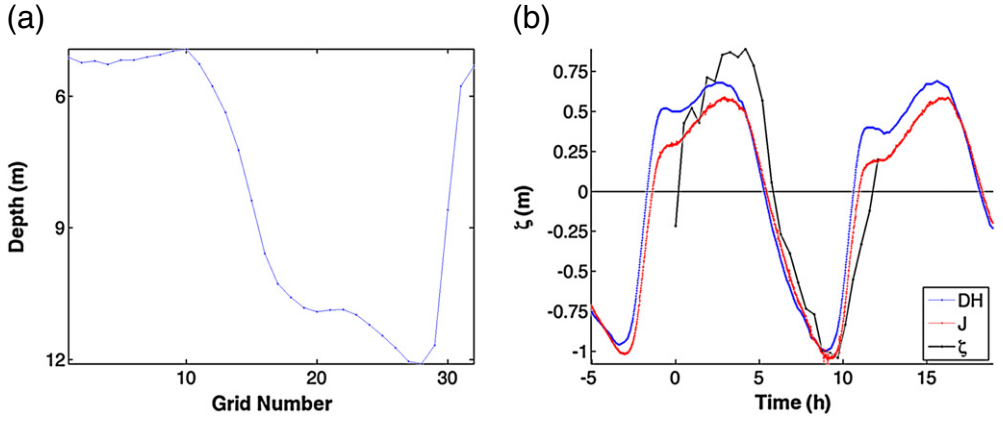

Fig. 3. (a) Tidally-averaged water depth $\tilde{H}$(m) at the 32 grid points. (b) Tidal sea surface elevation ζ(m), relative to longterm mean depth observed at MSI (black dots) and on shore, in Den Helder (DH, blue curve) and at Texel jetty (J, red), as a function of time t (h).

will use depth-averaged velocities to compute the circulation – and infer their relevance for the tidal dynamics in this area.

4. Results

Fig. 4 displays velocities in along-topography (55°T), cross-topography (325°T) and vertical direction (see legend for scale) as a function of depth and time on 6 October 2009. Over the tidal cycle, the vessel encounters water depth changes during each loop of about 30 min. On top of these, a slower tidal elevation change is encountered, leading to an apparent motion of the bottom of about 2 m, peak-to-peak. The velocity measurements show the dominance of semi-diurnal tidal motion, mainly taking place in the East–West direction. The weaker cross-isobath and mean flows that are also present in these measurements, as well as a decrease of tidal flow over the shallow part, will be discussed later on.

4.1. Tidal velocity

To estimate the amplitudes and phases of the semi-diurnal, quarter-diurnal and sixth-diurnal tidal velocity fields, as well as of the time-averaged currents, Harmonic Analysis (HA) is used in each vertical bin of each compartment. Mean and quarter-diurnal fields are considered to be generated by nonlinear advection, sixth-diurnal terms mainly by nonlinear bottom friction $\propto \mathbf{u}|\mathbf{u}|$. Zimmerman (1980) argues that the latter may also be due to vorticity advection by the background tidal current. The relatively large amplitude of the sixth-diurnal suggests that both bottom friction as well as vorticity advection are at play. Fig. 5 shows the harmonically analyzed, vertically-averaged velocity in each grid point.

The amplitudes (Fig. 5a) display an enhancement of the along-topography, depth-averaged flow (red lines) over the deep parts of the contour (grid points 17–29). The weakest along-topography tidal amplitudes are found at grid point 12, where the slope in topography is largest. Remarkably, the cross-topography, depth-averaged flow (black lines) is strongest at that location, possibly owing to refraction of the tidal wave. Refraction is due to the fact that the phase speed of the transmitted part of the long tidal wave is determined by the square root of water depth. Therefore the wave, as well as the direction of the tidal ellipse's major axis, veers toward the shoals. Fig. 5b shows that phases of the semi-diurnal and sixth-diurnal components are somewhat delayed over the deep channel compared to those over the shallow tidal-flat, grid points 2–14 (see Fig. 2). By contrast, in the channel the phase of the quarter-diurnal *leads* that over the shoals, identifying advective nonlinearity acting on the stronger tidal flow in the deeper channel as its source.

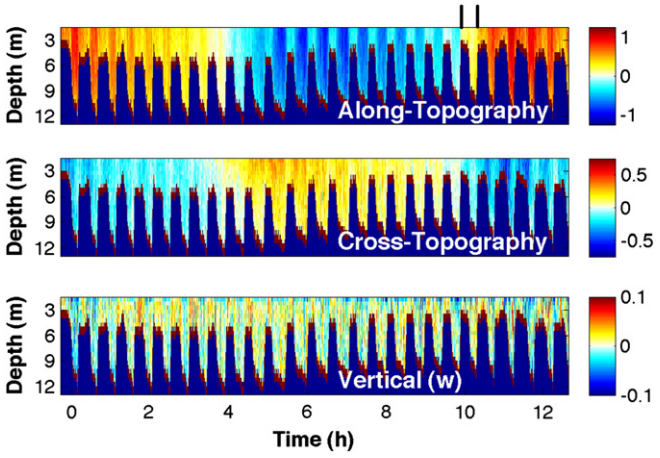

Fig. 4. Variation of along-topography (top panel), cross-topography (middle) and vertical (bottom) velocity (m s^{-1}) during the 26 cycles on 6 October 2009 as a function of time (h) and depth (m). Red areas near the bottom represent the 'blanking distance', where velocity observations are unreliable due to side-lobe interference. Positive values of along and cross-topography flows represent Wadden Sea inwards, and down-slope flows, respectively.

The depth-averaged semi-diurnal tide can be represented by an average over the number of vertical bins K_{ij} at point $\mathbf{x}_i$ during loop j, i.e., $\bar{\mathbf{u}}_{ij} = K_{ij}^{-1}\sum \mathbf{u}_{ijk}$. Another way of representing this is by means of tidal ellipses in grid points along the loop, Fig. 6a. The vertically-averaged along and cross-topography flow components averaged spatially over all grid points are displayed in Fig. 6b. This shows that during flood ($0<t<4$ h and $10<t<12.5$ h) the flow has an upslope (negative cross-slope) component, and vice versa during ebb. In Fig. 6a semi-diurnal ellipses are traversed in an *anti-clockwise* sense, indicating the dominance of the anticlockwise over the clockwise velocity component. One reason for this could be due to a difference of the anticlockwise (cyclonic, +) and clockwise (anti-cyclonic, –) Ekman-depths, $\delta_{\pm} = (2K/(\sigma \pm f))^{1/2}$, where K indicates a vertical eddy viscosity coefficient (assumed constant here), $\sigma = 1.406\times10^{-4}\,\mathrm{rad}\,s^{-1}$, the semi-diurnal tidal frequency, and $f = 1.164\times10^{-4}\,\mathrm{rad}\,s^{-1}$, the Coriolis parameter at the MSI's latitude of nearly 53°N. Since the latter two frequencies are close to each other, for a value of $K = 1.8\times10^{-2}\ m^2\ s^{-1}$, this implies $a_{\pm} = 8$ and 27 m, respectively. The eddy viscosity value, $K = C_d U_{\mathrm{rms}}^2/(200f)(1+7Ri)^{-1/4}$, is estimated following the analysis in Stanev et al. (2007), based on the root-mean-square velocity $U_{\mathrm{rms}} = 0.46\ m/s$, using that a vertical density difference $\Delta\rho = O(0.5kg\ m^{-3})$. Here $C_d = 2.5\times10^{-3}$ is the drag coefficient, $Ri = g'H/U_{\mathrm{rms}}^2$, the Richardson number, $g' = g\Delta\rho/\rho$ the reduced gravity, g the acceleration of gravity, $ho = 10^3 kg\ m^{-3}$ the average density, $f = 1.4\times10^{-4}$ the Coriolis frequency at latitude $52^{circ}N$ and $H \approx 10m$ the average depth. Thus, the anticyclonic component has a larger Ekman depth than the cyclonic component, $\delta_+ < \delta_-$. This means that the cyclonic component is less retarded within the water column, thus dominating their sum (Maas and van Haren, 1987; Prandle, 1982). When both rotary Ekman depths are much larger than local waterdepth, $\delta_{\pm} \gg H$, the whole water column is dominated by friction. Turning of the velocity vector is in that case suppressed and we recover the familiar result that rotational effects on the surface tide are absent. We note that suppression of Coriolis effects is caused by frictional layers being thicker than water depth, instead of by a limited width of the tidal channel per se — although these usually go hand-in-hand.

As indicated by the length of the major axes (see Fig. 6a), tidal velocities in the channel (grid points 17–29) are twice as large as over the shallow shelf. Tidal phase is advanced over the shallow part (indicated by the orientation of sticks inside the ellipses that are turned more clockwise), relative to those over the deeper parts. Both the decrease in tidal current amplitude, as well as the phase advance are indications of increased friction over the shallow regions. Apart from long wave refraction, friction is also responsible for the tendency of the major axis inclination to veer toward shallower water on approach of the bottom. In fact, the decrease in current strength toward the shoals suggests that friction dominates refraction. The strength of the tidal current and the generation of overtides by advective or frictional nonlinearities indicate tidal asymmetry. By means of tidal rectification, these terms are important for the generation of residual (tidally averaged) vorticity, or eddies, which play an important role in the dispersion of matter in the Wadden Sea (Beerens et al., 1994; Ridderinkhof and Zimmerman, 1992; Zimmerman, 1986).

Computing the along and cross-isobath semi-diurnal tidal velocity components as a function of depth reveals that within the channel, grid points 15–30 (see Fig. 7), tidal motion is nearly rectilinear over the whole water column yet displays vertical shear produced by bottom friction. There is a strong, vertically-sheared cross-topography motion over the South-Western slope of the contour along which the vessel travels (near grid point 12), but similar cross-topography motion lacks over the slope on the North-eastern part (grid point 31). Tidal phases of the along and cross-isobath flow components again show a phase advance over the shoals relative to the deep

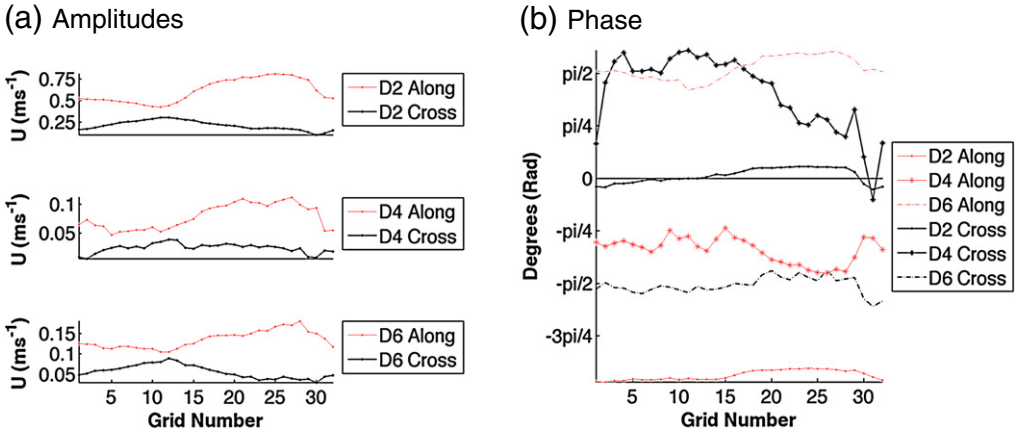

Fig. 5. (a) Tidal amplitudes U and (b) tidal phases of vertically-averaged, along-topography flow (red lines) and cross-topography flow (black lines) for semi-diurnal (D2, dots), quarter-diurnal (D4, stars) and sixth-diurnal (D6, dashed) velocity components.

channel. Such tidal phase advance due to frictional effects close to the bottom and over shoals was also observed in Lower Chesapeake Bay (Valle-Levinson and Lwiza, 1995).

4.2. Velocity–depth relation

Several simple theories make apparently contradictory predictions on how tidal amplitude varies as a function of local depth. The observed vertical structure of the horizontal velocity profile suggests which mechanism is dominant. In one interpretation, valid over deep-water, mass-conservation of the barotropic tidal flow predicts that over small scales, tidal transport, $\mathbf{Q}(\mathbf{t})$, is spatially constant: $H\mathbf{u}\equiv\mathbf{Q}$ (Baines, 1982). Thus, this predicts that the depth-averaged velocity is inversely proportional to local depth, $(u,v)=\mathbf{Q}/H(x,y)$.

In another interpretation, valid in shallow-water, frictional processes determine the tidal current strength and predict that velocity should vary linearly or parabolically with depth, $(u,v)\propto H$ or $H^{1/2}$, depending on the friction law being assumed linear or quadratic. This is more appropriate for the Wadden Sea, as suggested by the velocity observations in Fig. 4.

We can check this by plotting tidal harmonic amplitude $U\equiv(U_i^2+V_i^2)^{1/2}$ against local, tidally averaged water depth $\tilde{H}_i$, $i\in\{1,I\}$ (see Fig. 8). Here $\mathbf{U}_i$ indicates the tidal velocity magnitudes in x,y direction in the grid points at the centers of the 32 compartments that we defined in Fig. 2. This plot, of course, also has only 32 points, many of them either over shallow (5 m) or over deep (11–12 m) water. But, we clearly observe, as expected from Fig. 4, that the semi-diurnal velocity increases with depth, approximately linearly (see fit). As indicated before, there is also a phase advance of about 0.15 radians over the shallower parts, indicating that the tide turns earlier by about half an hour over the shallow parts, compared to the deep parts. Such a rapid change in tidal phase can be seen directly in the along-topography flow in Fig. 4a (see the two moments in time indicated by vertical bars above the figure). These rapid phase variations indicate the presence of large lateral shear in the tidal flow. It will turn out that these rapid variations of along-topography flow may jeopardize the accurate computation of net mass fluxes through the closed contour.

4.3. Mean flow

A contour average of the along and cross-topography flow shows that during flood (between 0–4 h and 10–12.5 h) the flow is upslope (negative cross-isobath motion) and during ebb downslope (see Fig. 6b). Asymmetry in these figures suggests that there is also a time-averaged flow. Indications for the existence of such a time-mean, cross-isobath circulation cell are evident in the average vertical velocity field, Fig. 9c. While vertical velocities are in general small and highly variable, the tidally averaged vertical velocity has a spatially coherent structure. It shows persistent upwelling over the shoals and downwelling over the deep channel. This may well be part of the residual, "rectified" circulation cell, driven by tidal motion over sloping topography (Zimmerman, 1978; (1980)). It may also be an indication of a persistent estuarine circulation cell. Due to fresh

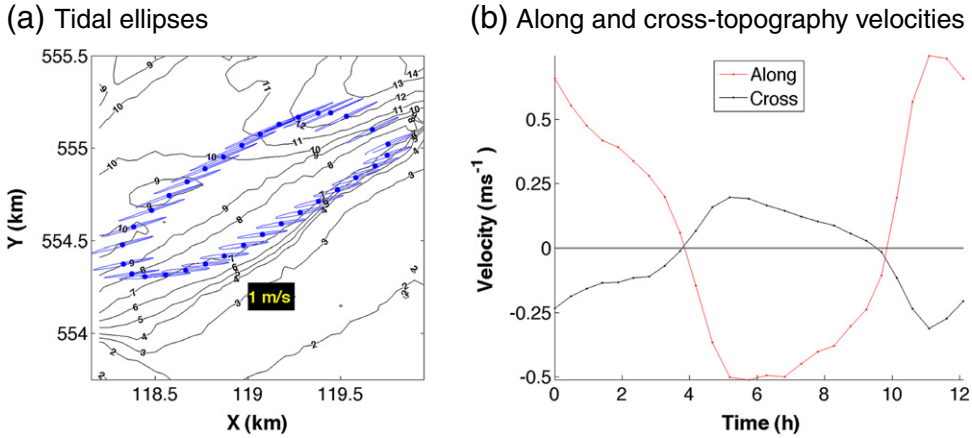

Fig. 6. (a) Semi-diurnal, vertically-averaged tidal ellipses obtained at grid points. Isobaths (black lines) show depth in m. (b) Contour-averaged along and cross-topography motions as a function of time (h).

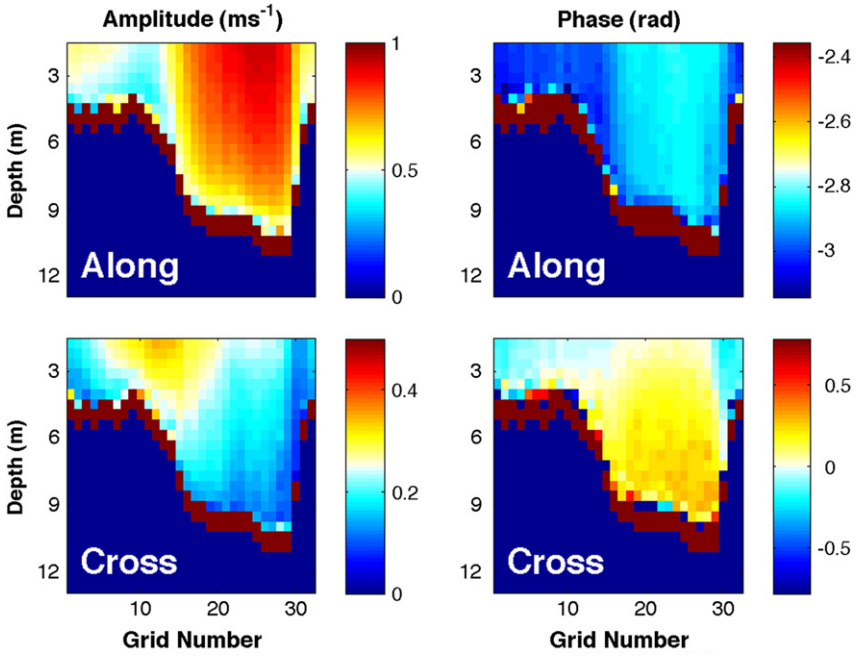

Fig. 7. Semi-diurnal amplitudes (left) and phases (right) of the flow ($m\,s^{-1}$) in along-topography (top panel) and cross-topography direction (bottom) as a function of grid point, horizontal axis and depth (m), vertical axis (see Fig. 2). Red color represents ADCP blanking distance.

water sources (river outflow), large-scale horizontal density differences occur in the Wadden Sea (Ridderinkhof and Zimmerman, 1992). The saltier water, originating in the deep channel, will be advected onto the shoals by cross-isobath tidal motion where it will be mixed. This leads to small-scale horizontal density differences. Thus it is natural to expect an estuarine type of circulation over the slope, in which fresher shelf water stretches out over the saltier channel water (Dronkers and Zimmerman, 1982). However, the corresponding cross-topography flow – upslope near the bottom and down-slope in the upper water column – while weakly visible, is overshadowed by a *persistent* up-slope cross-topography flow (see Fig. 9b). This strong upslope flow bears evidence of a flood surplus, an asymmetry between in and outflow encountered frequently in vigorous tidal areas. During flood, the strong inflow enters through flood channels and spills onto the adjacent shallow shelf and tidal flats, while during ebb the tidal outflow takes different routes, draining through ebb channel systems consisting of a network of small gullies and sinuous tidal channels (van Veen, 1950; van Veen et al., 2005). Such a flood surplus over the shoals is also observed in the East Wadden Sea and attributed to a tide induced Stokes drift (Stanev et al., 2007). This differs, however, from the dynamics in tidal areas where shoals are substantially deeper (Valle-Levinson and Lwiza, 1995).

Fig. 10a presents the horizontal time and depth-averaged mean flow, together with the bathymetry. It shows that a North-eastward, Wadden Sea-inward mean flow has a strong along-isobath component that increases in strength toward the edge of the shallow shelf (on its Southern side). This is the location where also the mean upslope cross-isobath flow is strongest. The existence of an along-isobath mean flow, having the shallow part of the topography at its right-hand side when looking downstream (Fig. 9a), is predicted by tidal rectification theories. It is attributed to three tidal rectification mechanisms.

Two mechanisms arise in models using depth-averaged velocities. These are due to tidal advection of tidally-induced vorticity, produced by Coriolis and bottom-frictional torques, respectively Zimmerman (1978). Assuming that friction induces a partial in-phase relationship between advecting flow and vorticity, a mean-flow is generated. For a topography that is rotated anticlockwise relative to the main tidal current direction (as in Fig. 6a), the two vorticity generation

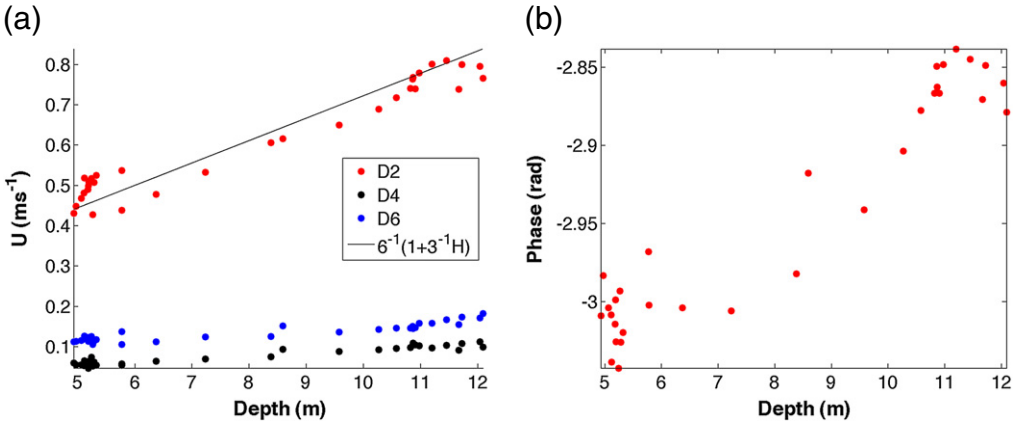

Fig. 8. (a) Tidal harmonic velocity amplitudes U for semi-diurnal (D2, red dots), quarter-diurnal (D4, black) and sixth-diurnal (D6, blue) components as a function of tidally averaged water depth $\bar{H}$ in m. Solid line gives a linear fit. (b) Same for semi-diurnal phase.

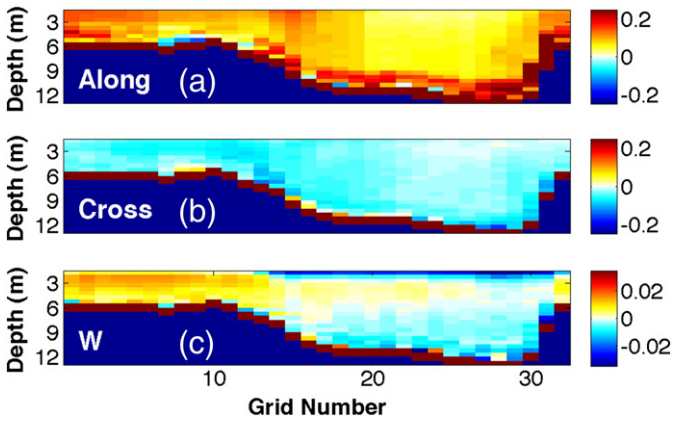

Fig. 9. Time-averaged velocity ($m\ s^{-1}$) observed at grid points along the vessel's time-averaged trajectory of (a) along topography, (b) cross-topography and (c) vertical velocity, w, as a function of depth (m).

mechanisms cooperate and reinforce one another, leading to the generation of a strong residual flow (Zimmerman, 1981a). The effect is proportional to topographic slope and is strongest when the cross-isobath excursion scale, $l_e \equiv v/\sigma$, is similar to the cross-isobath length scale, $l \approx 200\ m$. Over the contour traversed by the vessel, the cross-isobath, depth-averaged current, v, varies in intensity, Fig. 6a. Near the south end, the cross-isobath displacement, $l_e \gg l$, but in the Eastern part, where cross-isobath flow is less, these are of similar magnitude.

A third mechanism is due to a three-dimensional effect. It is concerned with the presence of vertical shear of the along-isobath horizontal tidal current, neglected in the previous two mechanisms. Due to the presence of a tidal cross-isobath circulation cell, the horizontal vorticity vector that points down-slope is tilted into the vertical direction (see Fig. 7). It thus acts as another driver of the time-averaged vertical vorticity field, one that is proportional to the topography's curvature (second derivative) (Zimmerman, 1981b).

4.4. Cross-contour transport and vorticity

Of central interest to the present study is the horizontal volume *transport* through the sides of the compartments – centered at $\mathbf{x}_i$ – that together form the closed loop. In each grid point, and for each loop, this transport is defined as the product of water depth, H_{ij}, the width of the compartments, L_i, and the depth-averaged velocity: $\mathbf{U}_{ij} \equiv H_{ij} L_i \bar{\mathbf{u}}_{ij}$. Here, $\bar{\mathbf{u}}$ now refers to the two horizontal velocity components only, and no summation is implied.

Fig. 10b represents transport $\mathbf{U}_{ij} \cdot \mathbf{n}_i$ as a function of grid number i and loop number (time) j. The first loop e.g. takes place during flood, having currents into a north-easterly direction (see Fig. 4a). Looking at this first loop, it is observed that the *net* transport during that loop, the net outwards (+) or inwards (−) directed transport, F_j, during the j-th circuit, computed according to

$$F_j = \sum_{i=1}^{I} \mathbf{U}_{ij} \cdot \mathbf{n}_i,$$

depends sensitively on the contributing transports U_{ij} per compartment. This is because within this sum essentially the difference between two large numbers is taken, representing a large inflow along the slope in the SW corner, near grid point 15, and a large outflow along the slope in the NE corner, near grid point 30. Details, like the precise orientation of the normal direction – highly variable in the two corners – the variability in effective depth over these two slopes, the length over which this normal flow acts (changing for subsequent vessel trajectories), and possibly the reliability of the ADCP measurement when the vessel is turning sharply, all become potential causes of errors in the determination of the cross-contour transport in subsequent compartments. Over these slopes, both the current amplitude as well as the phase vary rapidly. This might explain why it is rather difficult to capture net cross-contour transports accurately (see Fig. 11a, top).

By dividing the net transport through each contour by surface area $A = (6.5 \pm 0.4) \times 10^5 m^2$ enclosed by the loop, one determines the net vertical displacement, $\Delta\zeta$, over the time span of approximately 30 min during which the loop is 'circled'. Compared to the net change in sea-level taking place onshore over that same period (see Fig. 11b), we find that the transport-determination is still in need of improvement before this can be reliably applied to obtain net heat, nutrient or sediment fluxes through the encircled contour. The inferred change in water level, while of the same order of magnitude as that observed, is completely off, particularly at the end of the flood and beginning of the ebb-period (2–7 h).

Multiplying the along-contour, depth-averaged velocity by the compartment width, for each loop its contour-average, the net circulation $C = \oint \bar{\mathbf{u}} \cdot d\mathbf{s}$, can be computed. The time-evolution of this quantity is dominated by the semi-diurnal tide, apart from a (negative) residual circulation, $\tilde{C}$ (see Fig. 11a, bottom), where the tilde again indicates averaging over a tidal period. The circulation thus varies between $C = -150 \pm 350\ m^2\ s^{-1}$. By Green's theorem, the circulation

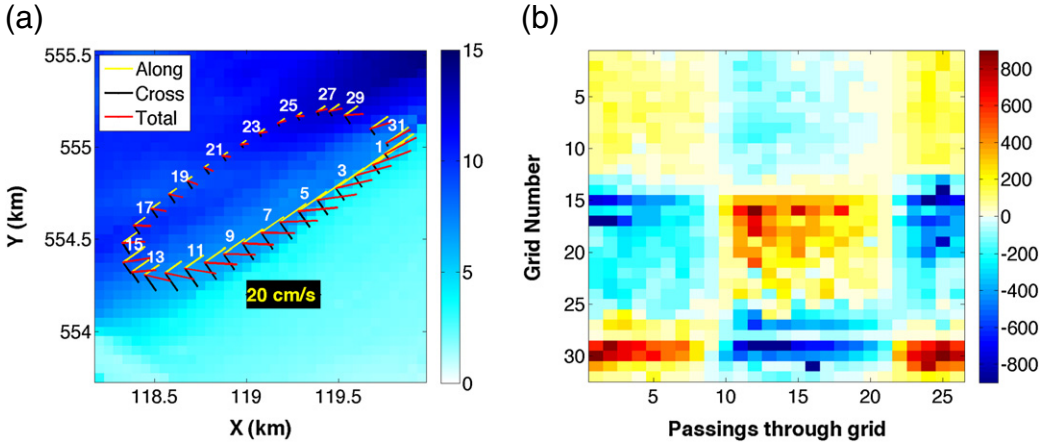

Fig. 10. (a) Tidally-averaged flow (red sticks) in grid points on 6 October 2009, averaged over a tidal cycle, and decomposed in along-topography (yellow) and cross-topography (black) components. (b) Cross-contour transport $\mathbf{U}_{ij} \cdot \mathbf{n}_i$ (color, in $m^3\ s^{-1}$) as a function of time (loop number) along abscissa, and grid number along ordinate.

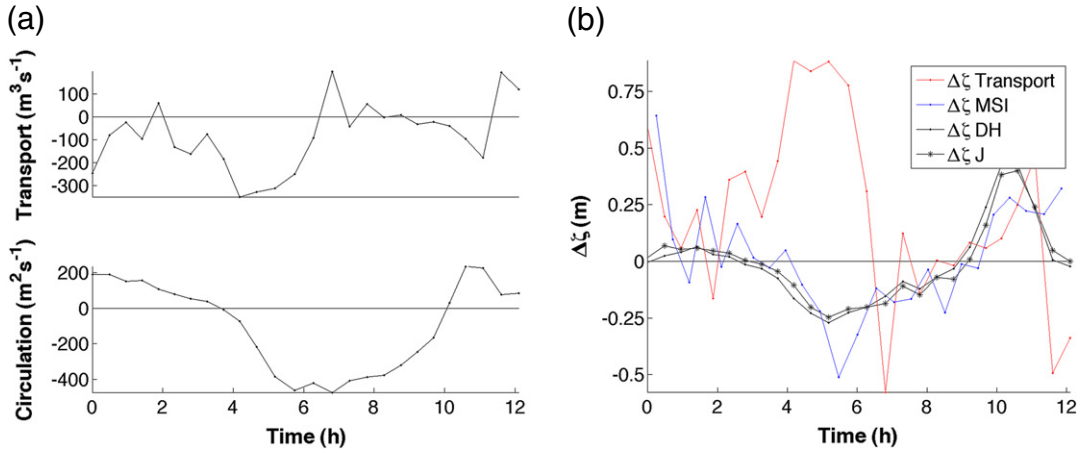

Fig. 11. (a) Time variation of cross-contour transport $\mathbf{U}_{ij}\cdot\mathbf{n}_i$ (top) and along-contour circulation C (bottom). (b) Sea surface height increase ($\Delta\zeta$) measured over duration of single loop, based on transport through the boundary of the contour (red), compared to sea surface elevation changes observed in Den Helder (DH), at the jetty on Texel (J) and at the MSI (blue).

is related to the vorticity ω, averaged over the area A enclosed by the contour, $C=\int\int\omega dA=[\omega]A$, where the brackets denote spatial averaging. The presence of large cyclonic (anticlockwise) residual vorticity, $[\bar{\omega}]=\bar{C}/A\approx 2.3\times10^{-4}\ s^{-1}$, in combination with the alternating advecting tide, is of great importance in promoting the dispersion of matter. In the context of the feeding of mussel seed, this is clearly a positive aspect in refreshing the waters over each tidal cycle, thereby suggesting that the MSI spot is well-chosen.

5. Discussion and conclusions

While the absence of mussel cultures renders application of the two integral theorems to estimate nutrient fluxes and tidal and tidally-averaged vorticity presently unfeasible, for future purposes we now indicate how Gauss' theorem can be applied to the advection–diffusion equation for nutrient concentration C. Here we exploit that with our 1 Hz sampling, there are about 58 measurements per compartment average (each compartment is visited every 30 min). Employing the incompressibility condition, and using Reynolds decomposition of the concentration and velocity fields, $C=<C>+C'$, and $\mathbf{u}=<\mathbf{u}>+\mathbf{u}'$, where $<C>$ and $<\mathbf{u}>$ denote compartment-averages and C' and $\mathbf{u}'$ their deviations, this equation is written in flux-form:

$$\frac{\partial<C>}{\partial t}+\nabla\cdot(<\mathbf{u}><C>)=-\nabla\cdot<\mathbf{u}'C'>-S. \quad (1)$$

This equation describes the rate of change of ensemble average concentration due to the divergences of advective (left hand), diffusive fluxes (right hand) and nutrient consumption, S. The important quantity is the correlation between turbulent velocity and concentration fluctuations, $<\mathbf{u}'C'>$, i.e., their compartment averaged product.

In theoretical works, the diffusive flux is normally related to the gradient of the ensemble average field, $<\mathbf{u}'C'>=-K_h\nabla<C>$, where K_h is a horizontal eddy diffusivity. But, applying such a parametrisation would require knowledge of the *transverse* gradient of the average concentration field, not offered by measurements *along* the contour. However, as velocity and concentration perturbations are simply measured along the contour, Eq. (1) can be used directly. Integrating this equation over the same fixed volume as described above, allows the total nutrient consumption by mussels $\int_V S\ dV$ to be determined from cross-contour fluxes and the time rate of change of the contour-averaged and ensemble-averaged concentration without the need for any parameterisation. In steady state, the ensemble average concentration field along the contour is constant and the flux alone determines the uptake by mussels. Note that this approach does require a frequency of measurements high enough to resolve for eddy diffusion time scales.

In the present work, however, no nutrients were measured and we considered hydrodynamic constraints only, that we will now summarize.

The change in sea surface height was obtained by averaging all measured water depths along each loop, subtracting the overall, tidally-averaged depth. Comparing to sea surface changes onshore shows some large deficiencies. These are attributed to the fact that, in the presence of a large overall water flux through the whole closed contour, we basically aim at measuring the difference between a very large inflow and a very large outflow, which is inherently 'problematic'. Significantly, the flux through any single curve segment (Fig. 10b) is much larger than the scale of the total flux, obtained upon summing these partial fluxes over all segments contributing to a single loop (Fig. 11a). This signals that small errors in the determination of the terms contributing to the flux, such as grid-depth, grid-length and the direction of the normal vector to the closed contour, may all be potentially important. Moreover, the presence of strong shear in the tidal currents presents an additional important source of errors. This shear is located precisely where the bottom slope is steepest and where the cross-contour tidal flow is largest. Spatial gradients and nonlinearities are thus largest near the shoulders of the shoals, in line with a similar observation in the lower Chesapeake Bay (Valle-Levinson and Atkinson, 1999). All these errors together inhibit a proper flux determination. Future work should address other methods for flux determination in the presence of strong through flows, especially as during slack the changes in flow conditions can be quite substantial over the 30 min duration taken by one loop.

For future application, we offer the suggestion that since the direct observation of the local sea surface elevation looks reliable compared to that onshore (Fig. 3b), this measurement can actually be used as a constraint on the divergence of the cross-contour currents. For, according to Gauss' divergence theorem, the volume integral of the divergence of the water flux – by the continuity equation, equal to the local time rate of change of the sea surface elevation – equals the surface integral of the mass-flux through the surface spanned by the closed contour and the bottom. The uncertainties in the aforementioned parameters, such as normal direction, water depth and grid-length, would allow optimizing these parameters such that the mass-balance is obeyed as good as possible. Since inaccuracies in the determination of the normal direction occur especially in the contour's sharp corners, we can weigh the uncertainty by local curvature of the contour. Alternatively, we could opt for sailing more circular

contours. Either way, incorporating this (weighted) global constraint would allow the use of the resulting normal current components to determine temperature and nutrient fluxes reliably.

In conclusion, we employed a new sampling strategy to determine volume fluxes into or out of a sea volume whose sides are determined by the vertical section between a closed contour traversed repeatedly by a ship and the sea bottom and mean sea surface. By employing Gauss' theorem, we were able to relate the volume flux into this volume with the vertical motion of the sea surface averaged over the area enclosed within the contour. Comparing the latter with direct sea surface elevation measurements provides us with a measure of the accuracy with which we can determine volume fluxes through this vertical section. With accurate measurements of nutrients, in the future this provides a useful method to determine a sink of nutrients within the encapsulated volume surrounding a Mussel Seed Installation. It turns out that under the circumstances of this particular experiment, it was not possible to obtain an accurate volume balance. Nonetheless we extracted the flaws of the method and make suggestions for successful future volume and nutrient flux determination. Other environmental factors determining the development of mussels concern the flushing and mixing of waters surrounding the MSI for which the tidal, tidally-averaged and estuarine circulation are all relevant. Green's theorem was used to obtain the area-averaged tidal and tidally-averaged vorticity from measurements of the circulation along the contour. It shows that from this perspective, the location of the MSI over a sharp topographic slope is well-chosen.

Acknowledgments

We thank Bert Brinkman (IMARES), for providing the incentive to perform the present analysis, Cor van Heerwaarden, for support during the cruises, and particularly Jeff Zimmerman for developing and sharing his ideas on Wadden Sea dynamics. We also thank Arnoldo Valle-Levinson, Huib de Swart and an unknown referee for making valuable suggestions for improvement. The Dutch Ministry of Transport, Public Works and Water Management (Rijkswaterstaat) is thanked for the use of their bathymetric data.

References

Baines, P.G., 1982. On internal tide generation models. Deep Sea Research Part A, Oceanographic Research Papers 29, 307–338.
Beerens, S.P., Ridderinkhof, H., Zimmerman, J.T.F., 1994. An analytical study of chaotic stirring in tidal areas. Chaos, Solitons and Fractals 4 (6), 1011–1029.
Dronkers, J., Zimmerman, J.T.F., 1982. Some principles of mixing in tidal lagoons. Oceanologica Acta, SP 4, 107–117 Suppl.
Groeskamp, S., Nauw, J.J., Maas, L.R.M., 2011. Observations of estuarine circulation and solitary internal waves in a highly energetic tidal channel. Ocean Dynamics, http://dx.doi.org/10.1007/s10236-011-0455-y.
Joyce, T.M., 1989. On in situ 'calibration' of shipboard adcps. Journal of Atmospheric and Oceanic Technology 6, 169–172.
Maas, L.R.M., van Haren, J.J.M., 1987. Observations on the vertical structure of tidal and inertial currents in the central north sea. Journal of Marine Research 45, 293–318.
Prandle, D., 1982. The vertical structure of tidal currents and other oscillatory flows. Continental Shelf Research 1 (2), 191–207.
Ridderinkhof, H., Zimmerman, J.T.F., 1992. Chaotic stirring in a tidal system. Science 258, 1107–1111.
Stanev, E.V., Flemming, B.W., Bartholomä, Staneva, J.V., Wolff, J.-O., 2007. Vertical circulation in shallow tidal inlets and back-barrier basins. Continental Shelf Research 27, 798–831.
Valle-Levinson, A., Atkinson, L.P., 1999. Spatial gradients in the flow over an estuarine channel. Estuaries 22, 179–193.
Valle-Levinson, A., Lwiza, K.M.M., 1995. The effects of channels and shoals on exchange between the chesapeake bay and the adjacent ocean. Journal of Geophysical Research 100, 18,551–18,563.
van Veen, J., 1950. Eb- en vloedscharen in de nederlandse getijwateren. Tijdschrift Koninklijk Nederlands Aardrijkskundig Genootschap 67, 43–65.
van Veen, J., van der Spek, A.J.F., Stive, M.J.F., Zitman, T., 2005. Ebb and flood channel systems in the netherlands tidal waters. Journal of Coastal Research 21, 1107–1120.
Zimmerman, J.T.F., 1978. Topographic generation of residual circulation by oscillatory (tidal) currents. Geophysical Astrophysical Fluid Dynamics 11, 35–47.
Zimmerman, J.T.F., 1980. Vorticity transfer by tidal currents over an irregular topography. Journal of Marine Research 38, 601–630.
Zimmerman, J.T.F., 1981a. Dynamics, diffusion and geomorphological significance of tidal residual eddies. Nature 290, 549–555.
Zimmerman, J.T.F., 1981b. Principal differences between 2d- and vertically averaged 3d-models of topographic tidal rectification. In: van de Kreeke, J. (Ed.), Physics of Shallow Estuaries and Bays. : Lecture Notes on Coastal and Estuarine Studies. Springer-Verlag, pp. 120–129.
Zimmerman, J.T.F., 1986. The tidal whirlpool: a review of horizontal dispersion by tidal and residual currents. Netherlands Journal Sea Research 20, 133–154.